

---

# Computer Simulation of Particle Suspensions

Jens Harting<sup>1</sup>, Martin Hecht<sup>1</sup>, Hans J. Herrmann<sup>2</sup>, and Sean McNamara<sup>1</sup>

<sup>1</sup> Institute for Computational Physics, University of Stuttgart, Pfaffenwaldring 27,  
70569 Stuttgart, Germany

`jens@icp.uni-stuttgart.de`

`Martin.Hecht@icp.uni-stuttgart.de`

`S.McNamara@icp.uni-stuttgart.de`

<sup>2</sup> Institute for Building Materials, ETH Hönggerberg, HIF E 12, 8093 Zürich,  
Switzerland

`hans@icp.uni-stuttgart.de`

**Summary.** Particle suspensions are ubiquitous in our daily life, but are not well understood due to their complexity. During the last twenty years, various simulation methods have been developed in order to model these systems. Due to varying properties of the solved particles and the solvents, one has to choose the simulation method properly in order to use the available compute resources most effectively with resolving the system as well as needed. Various techniques for the simulation of particle suspensions have been implemented at the Institute for Computational Physics allowing us to study the properties of clay-like systems, where Brownian motion is important, more macroscopic particles like glass spheres or fibers solved in liquids, or even the pneumatic transport of powders in pipes. In this paper we will present the various methods we applied and developed and discuss their individual advantages.

**Key words:** Particle suspensions, molecular dynamics, stochastic rotation dynamics, lattice Boltzmann method

## 1 Introduction

Adding a fluid to a dry granulate causes the behavior of the mixture to change dramatically and a host of unexpected phenomena arises. A good example can be studied by anyone on the beach: whereas it is impossible to build a sand castle from dry sand, once just a little bit of water has been stirred into the sand, one can shape the resulting material almost arbitrarily into surprisingly complex arrangements. Adding even more fluid might result in the material losing this stability. If we stir such a mixture, it behaves like a liquid of increased density. Other very common particle-fluid mixtures are ubiquitous in

our daily life and include the cacao drink which keeps separating into its constituents, tooth paste and wall paint which are mixtures of finely ground solid ingredients in fluids or blood which is made up of red and white blood cells suspended in a solvent. An extreme example is the sand on the beach which can be blown away by the wind. It is important for industrial applications to obtain a detailed knowledge of those systems in order to optimize production processes or to prevent accidents.

Long-range fluid-mediated hydrodynamic interactions often dictate the behavior of particle-fluid mixtures. The majority of analytical results for the particle scale behavior of suspensions has been obtained in the regime of vanishing Reynolds numbers (viscous flow). For large systems, scientists aim at an average, continuum description of the large-scale behavior. However, this requires time-consuming and sometimes very difficult experimental measurements of phenomenological quantities such as the mean settling speed of a suspension, the stress contributions in the system of the individual components (solid and fluid) as functions of, e.g., the solid volume fraction of the constituents.

Computer simulation methods are indispensable for many-particle systems, for the inclusion of inertia effects (Reynolds numbers  $> 1$ ) and Brownian motion (Peclet number of order 1). These systems often contain a large number of important time scales which differ by many orders of magnitude, but nevertheless have to be resolved by the simulation, leading to a large numerical effort. However, simulations have the potential to increase our knowledge of elementary processes and to enable us to find the aforementioned relations from simulations instead of experiments.

Various simulation methods have been developed to simulate particle-fluid mixtures. All of them have their inherent strengths but also some disadvantages. For example, simplified Brownian Dynamics does not contain long-ranged hydrodynamic interactions among particles at all [28]. Brownian Dynamics with full hydrodynamic interactions utilizes a mobility matrix which is based on tensor approximations which are exact in the limit of zero Reynolds number and zero particle volume fraction [57, 3]. However, the computational effort scales with the cube of the particle number due to the inversion of matrices. Pair-Drag simulations have been proposed by Silbert et al. [46], and include hydrodynamic interactions in an approximative way. They have focused on suspensions with high densities (up to 50%) of uncharged spherical colloidal particles. Stokesian Dynamics has been presented by Bossis and Brady in the 80s and applied by many authors [21, 1, 69, 34]. For example, Melrose and Ball have performed detailed studies of shear thickening colloids using Stokesian Dynamics simulations [36, 35]. However, this method is limited to Reynolds numbers close to zero and the computational effort is very high for dynamical simulations. Even with today's powerful computers it is not possible to study the dynamics of more than a few hundred particles. The method is still widely used due to its physical motivation and its robustness, but is complicated to code. Boundary-element methods are more flexible

than Stokesian dynamics and can also be used to simulate non-spherical or deformable particles, but the computational effort is even higher [48, 43].

All these methods assume that hydrodynamic interactions are fully developed and that the dynamics of the fluid and of the solved particles can be treated as fully separated. In reality, this is not the case. Hydrodynamic interactions are time dependent due to local stresses at the fluid-particle interfaces. A number of more recent methods attempt to describe the time dependent long-range hydrodynamics properly with the computational effort scaling linearly with the number of particles. These include recent mesoscopic methods like dissipative particle dynamics [14, 13, 7], the lattice-Boltzmann method [10, 43, 41, 42, 54, 38], or stochastic rotation dynamics [50, 51, 24, 23]. However, for small Reynolds numbers, the computational gain of these methods is lost due to the additional effort needed to describe the motion of the fluid. Finite element or finite difference methods need a proper meshing of the computational domain which is not trivial for complicated boundary conditions as in the case of dense suspensions. Therefore, many authors only simulated a limited number of static configurations rather than the full dynamics of the system. Advances in remeshing techniques as well as more powerful computers have allowed to overcome these problems. Also, in order to avoid remeshing at all, uniform grids can be used [16, 63, 25]. These methods are flexible and robust. They can properly treat non-Newtonian effects and incorporate inertia, but are complicated to code.

For a more detailed description of the simulation methods, experiments or theoretical approaches not addressed in this paper, the reader is referred to one of the various books on colloid science [49, 44, 64, 53, 62, 26].

The remainder of this paper focuses on three different simulation techniques which have recently been applied to particle-laden flows in our group. First, we introduce a method developed by Malevanets and Kapral to model a solvent with thermal fluctuations. This approach is used to study the properties of claylike colloids [24, 23]. For larger particles, thermal fluctuations are undesirable. Here, the lattice Boltzmann method and its extension to particle suspension is a very good candidate to study the dynamics of glass spheres in a sugar solution [38, 22]. The method is easy to code and has been applied to suspensions of spherical and non-spherical particles by various authors. If the particles are very massive and the density of the fluid is very low, a full hydrodynamic treatment of the solvent is not needed anymore. In the last chapter we describe an algorithm based on a coarse-grained description of the fluid, so that it is resolved on a length scale larger than the particles. Much larger systems can be treated this way, but the coarse-graining is justified only in certain situations. As an example we model the pneumatic transport of a powder in a pipe which is a common process in many industrial applications [52, 66, 67].

A more computational demanding and not as easy to code method is a Navier Stokes solver for the fluid which is coupled to the particles. The method has been successfully applied to the simulation of sedimentation processes

of spherical or non-spherical particles and profits from its well established physical background and long standing experience with similar fluid solvers in engineering disciplines [72, 63, 25, 40, 17, 18]. These methods have a long standing history in our group, but have been described in detail elsewhere and will not be covered in this paper.

## 2 Simulation of Claylike Colloids: Stochastic Rotation Dynamics

Dense suspensions of small strongly interacting particles are complex systems, which are rarely understood on the microscopic level. We investigate properties of dense suspensions and sediments of small spherical  $\text{Al}_2\text{O}_3$  particles by means of a combined Molecular Dynamics (MD) and Stochastic Rotation Dynamics (SRD) simulation. Stochastic Rotation Dynamics is a simulation method developed by Malevanets and Kapral [50, 51] for a fluctuating fluid. The work this chapter is dealing with is presented in more detail in references [24, 23].

We simulate claylike colloids, for which in many cases the attractive Van-der-Waals forces are relevant. They are often called “peloids” (Greek: clay-like). The colloidal particles have diameters in the range of some nm up to some  $\mu\text{m}$ . The term “*peloid*” originally comes from soil mechanics, but particles of this size are also important in many engineering processes. Our model systems of  $\text{Al}_2\text{O}_3$ -particles of about half a  $\mu\text{m}$  in diameter suspended in water are often used ceramics and play an important role in technical processes. In soil mechanics [59] and ceramics science [55], questions on the shear viscosity and compressibility as well as on porosity of the microscopic structure which is formed by the particles, arise [73, 47]. In both areas, usually high volume fractions ( $\Phi > 20\%$ ) are of interest. The mechanical properties of these suspensions are difficult to understand. Apart from the attractive forces, electrostatic repulsion strongly determines the properties of the suspension. Depending on the surface potential, one can either observe formation of clusters or the particles are stabilized in suspension and do sediment only very slowly. The surface potential can be adjusted by the *pH*-value of the solvent. Within Debye-Hückel theory one can derive a so-called  $2pK$  charge regulation model which relates the simulation parameters with the *pH*-value and ionic strength  $I$  adjusted in the experiment. In addition to the static interactions hydrodynamic effects are also important for a complete description of the suspension. Since typical Peclet numbers are of order one in our system, Brownian motion cannot be neglected.

## 2.1 Molecular Dynamics (MD): Simulation of the Suspended Particles

We study colloidal particles, composing the solid fraction, suspended in a fluid solvent. The colloidal particles are simulated with molecular dynamics (MD), whereas the solvent is modeled with stochastic rotation dynamics (SRD) as described in Sect. 2.2.

In the MD part of our simulation we include effective electrostatic interactions and van der Waals attraction, a lubrication force and Hertzian contact forces. In order to correctly model the statics and dynamics when approaching stationary states, realistic potentials are needed. The interaction between the particles is described by DLVO theory [28, 61, 47]. If the colloidal particles are suspended in a solvent, typically water, ions move into solution, whereas their counter ions remain in the particle due to a different resolvability. Thus, the colloidal particle carries a charge. The ions in solution are attracted by the charge on the particles and form the electric double layer. It has been shown (see [61]), that the resulting electrostatic interaction between two of these particles can be described by an exponentially screened Coulomb potential

$$V_{\text{Coul}} = \pi \varepsilon_r \varepsilon_0 \left[ \frac{2 + \kappa d}{1 + \kappa d} \cdot \frac{4k_B T}{ze} \tanh \left( \frac{ze\zeta}{4k_B T} \right) \right]^2 \times \frac{d^2}{r} \exp(-\kappa[r - d]), \quad (1)$$

where  $d$  denotes the particle diameter and  $r$  is the distance between the particle centers.  $e$  is the elementary charge,  $T$  the temperature,  $k_B$  the Boltzmann constant, and  $z$  is the valency of the ions of added salt. Within DLVO theory one assumes linear screening, mainly by one species of ions with valency  $z$  (e.g.  $z = +1$  for  $\text{NH}_4^+$ ). The first fraction in (1) is a correction to the original DLVO potential, which takes the surface curvature into account and is valid for spherical particles [6].

The effective surface potential  $\zeta$  is the electrostatic potential at the border between the diffuse layer and the compact layer, it may therefore be identified with *the*  $\zeta$ -potential. It includes the effect of the bare charge of the colloidal particle itself, as well as the charge of the ions in the Stern layer, where the ions are bound permanently to the colloidal particle. In other words, DLVO theory uses a renormalized surface charge. This charge can be related to the  $\text{pH}$  value of the solvent within Debye-Hückel theory [23].

$\varepsilon_0$  is the permittivity of the vacuum,  $\varepsilon_r$  the relative dielectric constant of the solvent.  $\kappa$  is the inverse Debye length defined by  $\kappa^2 = 8\pi\ell_B I$ , with the ionic strength  $I$  and the Bjerrum length  $\ell_B$ . We use 81 for water, which implies  $\ell_B = 7 \text{ \AA}$ .

The Coulomb term of the DLVO potential competes with the attractive van der Waals term

$$V_{\text{VdW}} = -\frac{A_H}{12} \left[ \frac{d^2}{r^2 - d^2} + \frac{d^2}{r^2} + 2 \ln \left( \frac{r^2 - d^2}{r^2} \right) \right]. \quad (2)$$

$A_H = 4.76 \cdot 10^{-20}$  J is the Hamaker constant [27] which involves the polarizability of the particles. It is kept constant in our simulations since it only depends on the material of the particles and on the solvent. The DLVO potentials are plotted in Fig. 1 for six typical examples with different depth of the secondary minimum. The primary minimum has to be modeled separately, as discussed below. Long range hydrodynamic interactions are taken

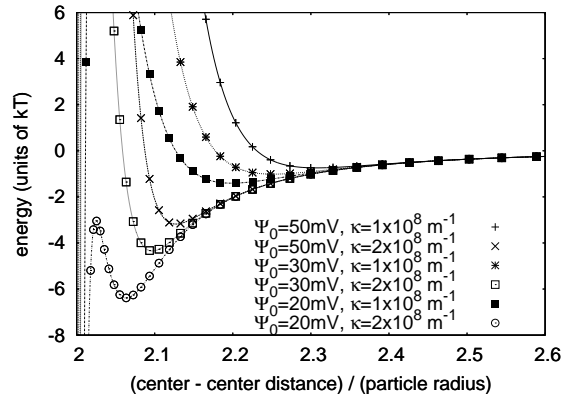


**Fig. 1.** DLVO potentials for  $\text{Al}_2\text{O}_3$  spheres of  $R = 0.5 \mu\text{m}$  diameter suspended in water. These are typical potentials used for our simulations as described below. The primary minimum at  $d/R = 2.0$  is not reproduced correctly by the DLVO theory. It has to be modeled separately. In most of our cases the existence of the secondary minimum determines the properties of the simulated system

into account in the simulation for the fluid as described below. This can only reproduce interactions correctly down to a certain length scale. On shorter distances, a lubrication force has to be introduced explicitly in the molecular dynamics simulation. The most dominant mode, the so-called squeezing mode, is an additional force

$$\mathbf{F}_{\text{lub}} = -(\mathbf{v}_{\text{rel}}, \hat{\mathbf{r}}) \hat{\mathbf{r}} \frac{6\pi\eta r_{\text{red}}^2}{r - r_1 - r_2}, \quad (3)$$

$$\text{with } r_{\text{red}} = \frac{r_1 r_2}{r_1 + r_2} \quad (4)$$

between two spheres with radii  $r_1, r_2$  and the relative velocity  $\mathbf{v}_{\text{rel}}$ .  $\eta$  is the dynamic viscosity of the fluid. In contrast to the DLVO potentials the lubrication force is a dissipative force. When two particles approach each other very closely, this force becomes very large. To ensure numerical stability of the simulation, one has to limit  $\mathbf{F}_{\text{lub}}$ . We do this by introducing a small cutoff radius  $r_{\text{sc}}$ . Instead of calculating  $\mathbf{F}_{\text{lub}}(r)$  we take the value for  $\mathbf{F}_{\text{lub}}(r + r_{\text{sc}})$ . In addition, since the force decays for large particle distances, we can introduce

a large cutoff radius  $r_{1c}$  for which we assume  $\mathbf{F}_{\text{lub}}(r) \equiv 0$  if  $r > r_{1c}$ . As the intention of  $\mathbf{F}_{\text{lub}}$  is to correct the finite resolution of the fluid simulation,  $r_{sc}$  and  $r_{1c}$  have to be adjusted in a way that the dynamic properties, i.e., the viscosity of a simulated particle suspension with weak DLVO interactions fit the measurements. It turns out that  $r_{sc} = 1.05(r_1 + r_2)$  and  $r_{1c} = 2.5(r_1 + r_2)$  work best.

To avoid that the particles penetrate each other, one needs a repulsive force depending on their overlap. We are using a Hertz force described by the potential

$$V_{\text{Hertz}} = K(d - r)^{5/2} \quad \text{if } r < d, \quad (5)$$

where  $K$  could be expressed by the elastic modulus of  $\text{Al}_2\text{O}_3$ . This would determine the simulation time step, but to keep the computational effort relatively small, we determine the time step using the DLVO-potentials as described later on and then choose a value for  $K$ . Two aspects have to be considered:  $K$  has to be big enough so that the particles do not penetrate each other by more than approximately 10% and it may not be too big, so that numerical errors are kept small, which is the case when the collision time is resolved with about 20 time steps. Otherwise total energy and momentum are not conserved very well in the collision.

The Hertz force also contains a damping term in normal direction,

$$\mathbf{F}_{\text{Damp}} = -(\mathbf{v}_{\text{rel}}, \hat{\mathbf{r}})\hat{\mathbf{r}}\beta\sqrt{r - r_1 - r_2}, \quad (6)$$

with a damping constant  $\beta$  and for the transverse direction a viscous friction proportional to the relative velocity of the particle surfaces is applied.

Since DLVO theory contains the assumption of linear polarizability, it holds only for large distances, i.e., the singularity when the two spheres touch does not exist in reality. Nevertheless, there *is* an energy minimum about  $30 k_{\text{B}}T$  deep, so that particles which come that close would very rarely become free again. To obtain numerical stability of our simulation, we model this minimum by a parabolic potential, some  $k_{\text{B}}T$  deep (e.g.  $6 k_{\text{B}}T$ ). The depth of the minimum in our model is much less than in reality, but the probability for particles to be trapped in the minimum has to be kept low enough so that only few of them might escape during simulation time.

For the integration of the translational motion we utilize a velocity Verlet algorithm [4] to update the velocity and position of particle  $i$  according to the equations

$$\mathbf{x}_i(t + \delta t) = \mathbf{x}_i(t) + \delta t \mathbf{v}_i(t) + \delta t^2 \frac{F_i(t)}{m}, \quad (7)$$

$$\mathbf{v}_i(t + \delta t) = \mathbf{v}_i(t) + \delta t \frac{F_i(t) + F_i(t + \delta t)}{2m}. \quad (8)$$

For the rotation, a simple Euler algorithm is applied:

$$\omega_i(t + \delta t) = \omega_i(t) + \delta t \mathbf{T}_i, \quad (9)$$

$$\vartheta_i(t + \delta t) = \vartheta_i(t) + F(\vartheta_i, \omega_i, \delta t), \quad (10)$$

where  $\omega_i(t)$  is the angular velocity of particle  $i$  at time  $t$ ,  $\mathbf{T}_i$  is the torque exerted by non central forces on the particle  $i$ ,  $\vartheta_i(t)$  is the orientation of particle  $i$  at time  $t$ , expressed by a quaternion, and  $F(\vartheta_i, \omega_i, \delta t)$  gives the evolution of  $\vartheta_i$  of particle  $i$  rotating with the angular velocity  $\omega_i(t)$  at time  $t$ . The concept of quaternions [4] is often used to calculate rotational motions in simulations, because the Euler angles and rotation matrices can easily be derived from quaternions. Using Euler angles to describe the orientation would give rise to singularities for the two orientations with  $\vartheta = \pm 90^\circ$ . The numerical problems related to this fact and the relatively high computational effort of a matrix inversion can be avoided using quaternions.

## 2.2 Stochastic Rotation Dynamics (SRD): Simulation of the Fluid

The Stochastic Rotation Dynamics method (SRD) introduced by Malevanets and Kapral [50, 51] is a promising tool for a coarse-grained description of a fluctuating solvent, in particular for colloidal and polymer suspensions. The method is also known as “Real-coded Lattice Gas” [33] or as “multi-particle-collision dynamics” (MPCD) [60]. It can be seen as a “hydrodynamic heat bath”, whose details are not fully resolved but which provides the correct hydrodynamic interaction among embedded particles [45]. SRD is especially well suited for flow problems with Peclet numbers of order one and Reynolds numbers on the particle scale between 0.05 and 20 for ensembles of many particles. The method is based on so-called fluid particles with continuous positions and velocities. Each time step is composed of two simple steps: One streaming step and one interaction step. In the streaming step the positions of the fluid particles are updated as in the Euler integration scheme known from Molecular Dynamics simulations:

$$\mathbf{r}_i(t + \tau) = \mathbf{r}_i(t) + \tau \mathbf{v}_i(t), \quad (11)$$

where  $\mathbf{r}_i(t)$  denotes the position of the particle  $i$  at time  $t$ ,  $\mathbf{v}_i(t)$  its velocity at time  $t$  and  $\tau$  is the time step used for the SRD simulation. After updating the positions of all fluid particles they interact collectively in an interaction step which is constructed to preserve momentum, energy and particle number. The fluid particles are sorted into cubic cells of a regular lattice and only the particles within the same cell are involved in the interaction step. First, their mean velocity  $\mathbf{u}_j(t') = \frac{1}{N_j(t')} \sum_{i=1}^{N_j(t')} \mathbf{v}_i(t)$  is calculated, where  $\mathbf{u}_j(t')$  denotes the mean velocity of cell  $j$  containing  $N_j(t')$  fluid particles at time  $t' = t + \tau$ . Then, the velocities of each fluid particle in cell  $j$  are updated as:

$$\mathbf{v}_i(t + \tau) = \mathbf{u}_j(t') + \mathbf{\Omega}_j(t') \cdot [\mathbf{v}_i(t) - \mathbf{u}_j(t')]. \quad (12)$$

$\mathbf{\Omega}_j(t')$  is a rotation matrix, which is independently chosen randomly for each time step and each cell. We use rotations about one of the coordinate axes by an angle  $\pm\alpha$ , with  $\alpha$  fixed. This has been suggested by M. Strauß in [70].



The coordinate axis as well as the sign of the rotation are chosen by random, resulting in six possible rotation matrices. The mean velocity  $\mathbf{u}_j(t)$  in the cell  $j$  can be seen as streaming velocity of the fluid at the position of the cell  $j$  at the time  $t$ , whereas the difference  $[\mathbf{v}_i(t) - \mathbf{u}_j(t)]$  entering the interaction step can be interpreted as a contribution to the thermal fluctuations.

In order to remove low temperature anomalies and to achieve exact Galilean-invariance, we use a modification of the original algorithm [29]: all particles are shifted by the *same* random vector with components in the interval  $[-a/2, a/2]$  before the collision step. Particles are then shifted back by the same amount after the collision. The random vectors of consecutive iterations are uncorrelated. Ihle and Kroll have discussed in [30, 31] why this simple procedure works and shown that it leads to transport coefficients independent of an imposed homogeneous flow field. In [32] and [37] analytical calculations of the transport coefficient of this method are presented.

Two different methods to couple the SRD and the MD simulation have been introduced in the literature. Inoue et al. proposed a way to implement no slip boundary conditions on the particle surface [33], whereas Falck et al. [15] have developed a “more coarse grained” method we describe shortly in the following section.

### 2.3 Coupling of the MD and the SRD Simulation Part

To couple the two parts of the simulation, MD on the one hand and SRD on the other one, the colloidal particles are sorted into the SRD boxes and their velocities are included in the rotation step. This technique has been used to model protein chains suspended in a liquid [15, 74]. Since the mass of the fluid particles is much smaller than the mass of the colloidal particles, one has to use the mass of each particle—colloidal or fluid particle—as a weight factor when calculating the mean velocity

$$\mathbf{u}_j(t') = \frac{1}{M_j(t')} \sum_{i=1}^{N_j(t')} \mathbf{v}_i(t) m_i, \quad (13)$$

$$\text{with } M_j(t') = \sum_{i=1}^{N_j(t')} m_i, \quad (14)$$

where we sum over all colloidal and fluid particles in the cell, so that  $N_j(t')$  is the total number of both particles together.  $m_k$  is the mass of the particle with index  $i$  and therefore  $M_j(t')$  gives the total mass contained in cell  $j$  at the time  $t' = t + \tau$ .

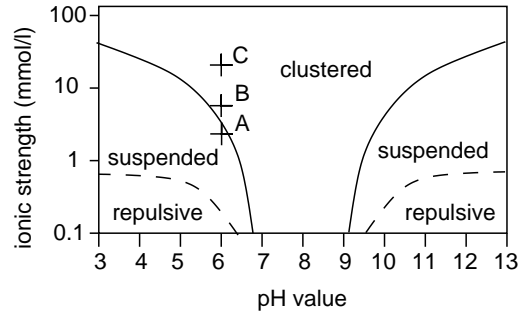


**Fig. 2.** Schematic phase diagram for volume fraction  $\Phi = 35\%$  in terms of  $pH$ -value and ionic strength involving three different phases: a clustering regime due to van der Waals attraction, stable suspensions where the charge of the colloidal particles prevents clustering, and a repulsive structure for further increased electrostatic repulsion. This work concentrates on state  $A$  ( $pH = 6$ ,  $I = 3$  mmol/l) in the suspended phase, state  $B$  ( $pH = 6$ ,  $I = 7$  mmol/l) close to the phase border but already in the clustered phase, and state  $C$  ( $pH = 6$ ,  $I = 25$  mmol/l) in the clustered phase [23]

## 2.4 Results

### Phase Diagram

Depending on the experimental conditions, one can obtain three different phases: A clustered region, a suspended phase, and a repulsive structure. These phases can be reproduced in the simulations and we can quantitatively relate interaction potentials to certain experimental conditions. A schematic picture of the phase diagram is shown in Fig. 2. Close to the isoelectric point ( $pH = 8.7$ ), the particles form clusters for all ionic strengths since they are not charged. At lower or higher  $pH$  values one can prepare a stable suspension for low ionic strengths because of the charge, which is carried by the colloidal particles. At even more extreme  $pH$  values, one can obtain a repulsive structure due to very strong electrostatic potentials (up to  $\zeta = 170$  mV for  $pH = 4$  and  $I = 1$  mmol/l, according to our model). The repulsive structure is characterized by an increased shear viscosity. In the following we focus on three states: State  $A$  ( $pH = 6$ ,  $I = 3$  mmol/l) is in the suspended phase, state  $B$  ( $pH = 6$ ,  $I = 7$  mmol/l) is a point already in the clustered phase but still close to the phase border, and state  $C$  ( $pH = 6$ ,  $I = 25$  mmol/l) is located well in the clustered phase.

Some typical examples for the different phases are shown in Figs. 3a)–d). These examples are meant to be only illustrative and do not correspond exactly to the cases  $A$ – $C$  in Fig. 2 denoted by uppercase letters. In the suspended case (a), the particles are mainly coupled by hydrodynamic interactions. One can find a linear velocity profile and a slight shear thinning. If one increases

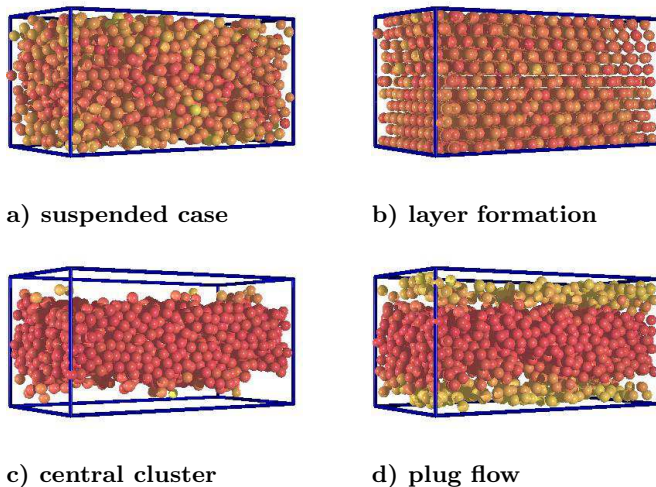


**Fig. 3.** Images of four different cases. For better visibility we have chosen smaller systems than we usually use for the calculation of the viscosity. The colors denote velocities: Dark particles are slow, bright ones move fast. The potentials do not correspond exactly to the cases *A–C* in Fig. 2, but they show qualitatively the differences between the different states: **a)** Suspension like in state *A*, at low shear rates. **b)** Layer formation, which occurs in the repulsive regime, but also in the suspension (state *A*) at high shear rates. **c)** Strong clustering, like in state *C*, so that the single cluster in the simulation is deformed. **d)** Weak clustering close to the phase border like in state *B*, where the cluster can be broken into pieces, which follow the flow of the fluid (plug flow)

the shear rate  $\dot{\gamma} > 500/\text{s}$ , the particles arrange in layers. The same can be observed if the Debye-screening length of the electrostatic potential is increased (b), which means that the solvent contains less ions ( $I < 0.3 \text{ mmol/l}$ ) to screen the particle charges. On the other hand, if one increases the salt concentration, electrostatic repulsion is screened even more and attractive van der Waals interaction becomes dominant ( $I > 4 \text{ mmol/l}$ ). Then the particles form clusters (c), and viscosity rises. A special case, called “plug flow”, can be observed for high shear rates, where it is possible to tear the clusters apart and smaller parts of them follow with the flow of the solvent (d). This happens in our simulations for  $I = 25 \text{ mmol/l}$  (state *C*) at a shear rate of  $\dot{\gamma} > 500/\text{s}$ . However, as long as there are only one or two big clusters in the system, it is too small to expect quantitative agreement with experiments. In these cases we have to focus on state *B* ( $I = 7 \text{ mmol/l}$ ) close to the phase border.

We restrict ourselves to the region around  $\text{pH} = 6$  where we find the phase border between the suspended region and the clustered regime at about  $I = 4 \text{ mmol/l}$  in the simulations as well as in the experiments. Also the shear

rate dependence of the viscosity is comparable in simulations and experiments as discussed below.

### Shear Profile and Shear Viscosity

In each of the three phases a typical velocity profile of the shear flow occurs. In the suspended phase one finds a linear velocity profile (Fig. 4a)) with nearly Newtonian flow. The particles are distributed homogeneously, thus the density profile is structureless (Fig. 5a)). The motion of the particles is only weakly coupled by the hydrodynamic forces. At high enough shear rates ( $\dot{\gamma} > 500$ ) the particles arrange in layers parallel to the shear plane, as can be seen in the density profile Fig. 5b), too. This arrangement minimizes collisions between the particles. As a result, the shear viscosity descends as shown in Fig. 6, which we discuss in more detail below. Shear induced layer formation has been reported in literature for different systems. Vermant and Solomon have reviewed this topic recently [71].

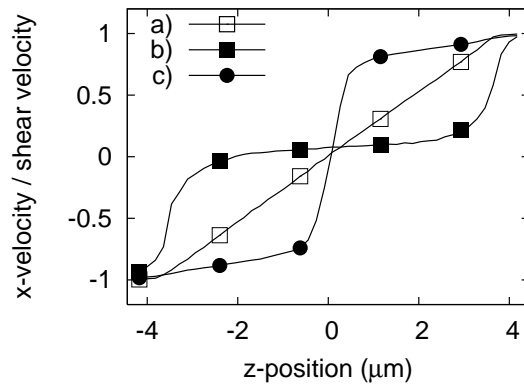


**Fig. 4.** Profiles of tangential velocity component in normal direction: a) Linear profile in the suspended regime, state *A* of Fig. 2 ( $I = 3$  mmol/l) at  $\dot{\gamma} = 500$ /s) b) Cluster formation in state *C* ( $I = 25$  mmol/l) at  $\dot{\gamma} = 100$ /s. In principle one could determine the viscosity of one single cluster from the central plateau, but this is not the viscosity found in experiments. There, one measures the viscosity of a paste consisting of many of these clusters c) Same as case b) but with higher shear rate (500/s). Hydrodynamic forces are large enough to break the cluster into two pieces. The velocity axis is scaled with the shear velocity  $v_S$  for better comparability

In the clustered phase, the clusters move in the fluid as a whole. They are deformed, but since the inter-particle forces are stronger than the hydrodynamic forces, the cluster moves more like a solid body than like a fluid.

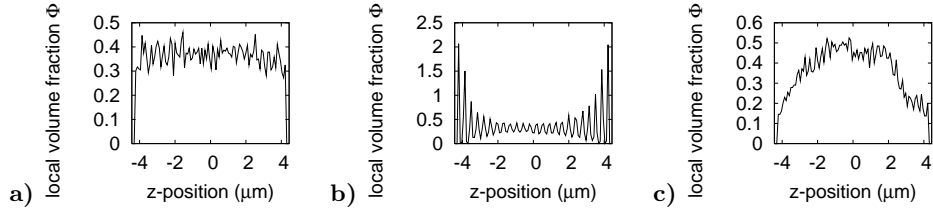


**Fig. 5.** Density profiles: **a)** Suspended case: State *A* in Fig. 2 ( $I = 3 \text{ mmol/l}$ ), at low shear rates ( $\dot{\gamma} = 50/\text{s}$ ). The density distribution is homogeneous **b)** Shear induced layer formation: This is state *A* as in graph a) of this figure, but for a high shear rate ( $\dot{\gamma} = 1000/\text{s}$ ) **c)** Strong attractive forces in state *C* ( $I = 25 \text{ mmol/l}$ ): For low shear rates ( $\dot{\gamma} = 50/\text{s}$ ) only one central cluster is formed, which is deformed slowly

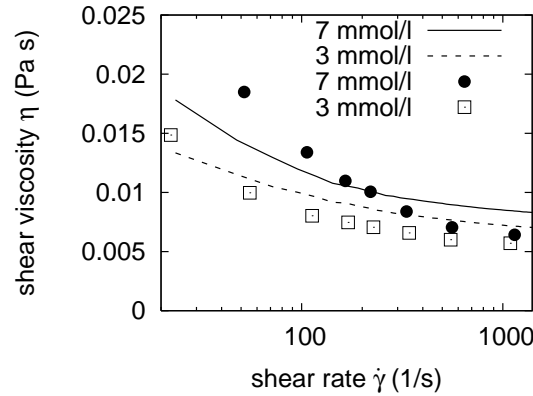


**Fig. 6.** Comparison between simulation and experiment: viscosity in dependence of the shear rate for the states *A* ( $I = 3 \text{ mmol/l}$ ) and *B* ( $I = 7 \text{ mmol/l}$ ) of Fig. 2. Note: shear thinning is more pronounced for the slightly attractive interactions in state *B* than for the suspended state *A*. Lines denote experimental data [58], points are results from our simulations

Often there is one big cluster that spans the whole system. The density profile (Fig. 5c)) increases in the central region and decays at the regions close to the border, since particles from there join the central cluster. When averaging the velocity profile in the shear flow, one finds a very small velocity gradient in the center of the shear cell and fast moving particles close to the wall, where the shear is imposed (Fig. 4b)). The velocity profile is non-linear on the length scale of the simulations. In the experiment the physical dimensions are much larger and therefore the velocity profile can become approximately linear again if the system consists of many large clusters. However, due to

the computational effort in simulations it is today impossible to measure the shear viscosity for these strongly inhomogeneous systems.

Closer to the phase border clusters can then be broken up into small pieces by the hydrodynamic forces at least for high shear rates. In state *C* of Fig. 2 this happens for the first time at  $\dot{\gamma} = 500/\text{s}$ , so that one can find two clusters in the system moving in opposite directions. The velocity profile of this case is shown in Fig. 4c). For even higher shear rates or closer to the phase border (e.g. state *B*), the clusters are broken into smaller pieces. Then, they move in the shear flow with an approximately linear velocity profile. Due to van der Waals attraction the system resists with stronger shear forces and the viscosity is higher than in the suspended case (Fig. 6).

In Fig. 6 the simulation results are shown together with the experimental results, both for the two cases of a slightly clustered system in state *B* ( $I = 7 \text{ mmol/l}$ ) and a suspension (state *A*,  $I = 3 \text{ mmol/l}$ ). For the suspension (state *A*) the viscosity decreases with the shear rate (“shear thinning”). The experimental data and the simulation are consistent within the accuracy of our model. There are several reasons for which our model does not fit exactly the measurements: Even though we use a charge regulation model to determine the input parameters for the DLVO potentials, microscopic properties like the surface density of sites, where ions can be adsorbed on the surface of the colloidal particle, have to be determined indirectly. Measurements of the  $\zeta$ -potential in certain conditions provide data to fit the unknown microscopic parameters. Furthermore, we have monodisperse spheres, which is another simplification in our model.

For the slightly clustered case (state *B*) an increase of the shear viscosity, compared to the suspended case, can be observed in the experiment as well as in the simulations. Shear thinning becomes more pronounced, because clusters are broken up, as mentioned above. However, the shear rate dependence is stronger in the simulations than in the experiment. This can be the first indication of finite size effects. We have studied the dependence of the simulated shear viscosity in dependence of the system size. The effect is most important for low shear rates.

### 3 Transport Phenomena and Structuring in Suspensions: Lattice-Boltzmann Simulations

For industrial applications, systems with rigid boundaries, e.g. a pipe wall, are of particular interest since structuring effects might occur in the solid fraction of the suspension. Such effects are known from dry granular media resting on a plane surface or gliding down an inclined chute [56, 68]. In addition, the wall causes a demixing of the solid and fluid components which might have an unwanted influence on the properties of the suspension. Near the wall one finds a thin lubrication layer which contains almost no particles and causes a

so-called ‘‘pseudo wall slip’’. Due to this slip the suspension can be transported substantially faster and less energy is dissipated.

We expect structuring close to a rigid wall at much smaller concentrations than in granular media because of long-range hydrodynamic interactions. In [38], we study these effects by the means of particle volume concentrations versus distance to the wall.

### 3.1 The Lattice-Boltzmann Method

The lattice-Boltzmann method is a simple scheme for simulating the dynamics of fluids. By incorporating solid particles into the model fluid and imposing the correct boundary condition at the solid/fluid interface, colloidal suspensions can be studied. Pioneering work on the development of this method has been done by Ladd et al. [41, 42, 43] and we use their approach to model sheared suspensions near solid walls.

The lattice-Boltzmann (hereafter LB) simulation technique which is based on the well-established connection between the dynamics of a dilute gas and the Navier-Stokes equations [9]. We consider the time evolution of the one-particle velocity distribution function  $n(\mathbf{r}, \mathbf{v}, t)$ , which defines the density of particles with velocity  $\mathbf{v}$  around the space-time point  $(\mathbf{r}, t)$ . By introducing the assumption of molecular chaos, i.e. that successive binary collisions in a dilute gas are uncorrelated, Boltzmann was able to derive the integro-differential equation for  $n$  named after him [9]

$$\partial_t n + \mathbf{v} \cdot \nabla n = \left( \frac{dn}{dt} \right)_{coll}, \quad (15)$$

where the left hand side describes the change in  $n$  due to collisions.

The LB technique arose from the realization that only a small set of discrete velocities is necessary to simulate the Navier-Stokes equations [20]. Much of the kinetic theory of dilute gases can be rewritten in a discretized version. The time evolution of the distribution functions  $n$  is described by a discrete analogue of the Boltzmann equation [43]:

$$n_i(\mathbf{r} + \mathbf{c}_i \Delta t, t + \Delta t) = n_i(\mathbf{r}, t) + \Delta_i(\mathbf{r}, t), \quad (16)$$

where  $\Delta_i$  is a multi-particle collision term. Here,  $n_i(\mathbf{r}, t)$  gives the density of particles with velocity  $\mathbf{c}_i$  at  $(\mathbf{r}, t)$ . In our simulations, we use 19 different discrete velocities  $\mathbf{c}_i$ . The hydrodynamic fields, mass density  $\varrho$ , momentum density  $\mathbf{j} = \varrho \mathbf{u}$ , and momentum flux  $\Pi$ , are moments of this velocity distribution:

$$\varrho = \sum_i n_i, \quad \mathbf{j} = \varrho \mathbf{u} = \sum_i n_i \mathbf{c}_i, \quad \Pi = \sum_i n_i \mathbf{c}_i \mathbf{c}_i. \quad (17)$$

We use a linear collision operator,

$$\Delta_i(r, t) = M_{ij}(n_j - n_j^{eq}), \quad (18)$$

where  $M_{ij} \equiv \frac{\partial \Delta_i(n^{eq})}{\partial n_j}$  is the collision matrix and  $n_i^{eq}$  the equilibrium distribution [10], which determines the scattering rate between directions  $i$  and  $j$ . For mass and momentum conservation,  $M_{ij}$  satisfies the constraints

$$\sum_{i=1}^M M_{ij} = 0, \quad \sum_{i=1}^M \mathbf{e}_i M_{ij} = 0. \quad (19)$$

We further assume that the local particle distribution relaxes to an equilibrium state at a single rate  $\tau$  and obtain the lattice BGK collision term [5]

$$\Delta_i = -\frac{1}{\tau}(n_i - n_i^{eq}). \quad (20)$$

By employing the Chapman-Enskog expansion [9, 19] it can be shown that the equilibrium distribution

$$n_i^{eq} = \varrho \omega^{c_i} \left[ 1 + 3\mathbf{c}_i \cdot \mathbf{u} + \frac{9}{2}(\mathbf{c}_i \cdot \mathbf{u})^2 - \frac{3}{2}u^2 \right], \quad (21)$$

with the coefficients of the three velocities

$$\omega^0 = \frac{1}{3}, \quad \omega^1 = \frac{1}{18}, \quad \omega^{\sqrt{2}} = \frac{1}{36}, \quad (22)$$

and the kinematic viscosity [43]

$$\nu = \frac{\eta}{\varrho_f} = \frac{2\tau - 1}{9}, \quad (23)$$

properly recovers the Navier-Stokes equations

$$\frac{\partial u}{\partial t} + (u \nabla) u = -\frac{1}{\varrho} \nabla p + \frac{\eta}{\varrho} \Delta u, \quad \nabla u = 0. \quad (24)$$

### 3.2 Fluid-Particle Interactions

To simulate the hydrodynamic interactions between solid particles in suspensions, the lattice-Boltzmann model has to be modified to incorporate the boundary conditions imposed on the fluid by the solid particles. Stationary solid objects are introduced into the model by replacing the usual collision rules (Equation (20)) at a specified set of boundary nodes by the “link-bounce-back” collision rule [54]. When placed on the lattice, the boundary surface cuts some of the links between lattice nodes. The fluid particles moving along these links interact with the solid surface at boundary nodes placed halfway along the links. Thus, a discrete representation of the surface is obtained, which becomes more and more precise as the surface curvature gets smaller and which is exact for surfaces parallel to lattice planes.



Since the velocities in the lattice-Boltzmann model are discrete, boundary conditions for moving suspended particles cannot be implemented directly. Instead, we can modify the density of returning particles in a way that the momentum transferred to the solid is the same as in the continuous velocity case. This is implemented by introducing an additional term  $\Delta_b$  in (16) [41]:

$$\Delta_{b,i} = \frac{2\omega^{c_i}\rho_i\mathbf{u}_i \cdot \mathbf{c}_i}{c_s^2}, \quad (25)$$

with  $c_s$  being the velocity of sound and coefficients  $\omega^{c_i}$  from (22).

To avoid redistributing fluid mass from lattice nodes being covered or uncovered by solids, we allow interior fluid within closed surfaces. Its movement relaxes to the movement of the solid body on much shorter time scales than the characteristic hydrodynamic interaction [41].

If two particle surfaces approach each other within one lattice spacing, no fluid nodes are available between the solid surfaces. In this case, mass is not conserved anymore since boundary updates at each link produce a mass transfer  $\Delta_b a^3$  ( $a \equiv$  cell size) across the solid-fluid interface [41]. The total mass transfer for any closed surface is zero, but if some links are cut by two surfaces, no solid-fluid interface is available anymore. Instead, the surface of each particle is not closed at the solid-solid contacts anymore and mass can be transferred in-between suspended particles. Since fluid is constantly added or removed from the individual particles, they never reach a steady state. In such cases, the usual boundary-node update procedure is not sufficient and a symmetrical procedure which takes account of both particles simultaneously has to be used [42]. Thus, the boundary-node velocity is taken to be the average of that computed from the velocities of each particle. Using this velocity, the fluid populations are updated (Equation (25)), and the force is computed; this force is then divided equally between the two particles.

If two particles are in near contact, the fluid flow in the gap cannot be resolved by LB. For particle sizes used in our simulations ( $R < 5a$ ), the lubrication breakdown in the calculation of the hydrodynamic interaction occurs at gaps less than  $0.1R$  [54]. This effect “pushes” particles into each other.

To avoid this force, which should only occur on intermolecular distances, we use a lubrication correction method described in [54]. For each pair of particles a force

$$\mathbf{F}_{\text{lub}} = -6\pi\eta \frac{R_1 R_2}{(R_1 + R_2)^2} \left( \frac{1}{h} - \frac{1}{h_N} \right) \mathbf{u}_{12} \cdot \frac{\mathbf{r}_{12}}{|\mathbf{r}_{12}|}, \quad h < h_N \quad (26)$$

is calculated, where  $\mathbf{u}_{12} = \mathbf{u}_1 - \mathbf{u}_2$ ,  $h = |\mathbf{r}_{12}| - R_1 - R_2$  is the gap between the two surfaces and a cut off distance  $h_N = \frac{2}{3}a$  [43]. For particle-wall contacts we apply the same formula with  $R_2 \rightarrow \infty$  and  $h = |\mathbf{r}_{12}| - R_1$ . The tangential lubrication can also be taken into account, but since it has a weaker logarithmic divergence and its breakdown does not lead to serious problems, we do not include it in our simulations.

### 3.3 Particle Motion

The particle position and velocity are calculated using Newton’s equations in a similar manner as in section on SRD simulations. To avoid repetition, the reader is referred to Sect. 2.1. However, particles do not feel electrostatic interactions, but behave like hard spheres in the case presented in this section.

### 3.4 Simulations

The purpose of our simulations is the reproduction of rheological experiments on computers. We simulate a representative volume element of the experimental setup and compare our calculations with experimentally accessible data, i.e. density profiles, time dependence of shear stress and shear rate. We also get experimentally inaccessible data from our simulations like translational and rotational velocity distributions, particle-particle and particle-wall interaction frequencies. The experimental setup consists of a rheoscope with two spherical plates, which distance can be varied. The upper plate can be rotated either by exertion of a constant force or with a constant velocity, while the complementary value is measured simultaneously. The material between the rheoscope plates consist of glass spheres suspended in a sugar-water solution. The radius of the spheres varies between 75 and 150  $\mu\text{m}$ . For our simulations we assume an average particle radius of 112.5  $\mu\text{m}$ . The density and viscosity of the sugar solution can also be changed. We simulate only the behavior of a representative volume element which has the experimental separation between walls, but a much lower extension in the other two dimensions than the experiment. In these directions we employ periodic boundary conditions for particles and for the fluid.

Shearing is implemented using the “link-bounce-back” rule with an additional term  $\Delta_{b,i}$  at the wall in the same way as already described for particles (Equation (25) with  $\mathbf{u}_i$  now being the velocity of the wall).

To compare the numerical and experimental results, we need to find characteristic dimensionless quantities of the experiment which then determine the simulation parameters. For this purpose we use the ratio of the rheoscope height and the particle size  $\lambda$ , the particle Reynolds number  $\Re$  and the volume fraction of the particles  $\phi$ . The simulation results are provided with units by calculating the length of the lattice constant  $a$  and the duration of one time step as described in [38].

### 3.5 Results

Figure 7 shows a snapshot of a suspension with 50 spheres after 5772500 time steps which are equivalent to 729 s. The vector  $\mathbf{g}$  represents the direction of gravity and  $\mathbf{v}_S$  depicts the velocity of the sheared wall.

The particles feel a gravitational acceleration  $g = 0.8 \text{ m/s}^2$ , have a mass  $m = 7.7 \cdot 10^{-8} \text{ kg}$ , a Reynolds number  $\Re = 4.066875 \cdot 10^{-4}$ , and a radius

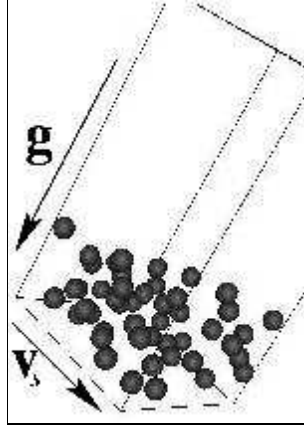


**Fig. 7.** A snapshot of a suspension with 50 spheres (radius  $R = 1.125 \cdot 10^{-4}$  m, mass  $m = 7.7 \cdot 10^{-8}$  kg) at time  $t = 729$  s. The volume of the simulated system is  $1.83 \cdot 10^{-3} \times 1.83 \cdot 10^{-3} \times 3.375 \cdot 10^{-3}$  m =  $11.3025 \cdot 10^{-9}$  m<sup>3</sup>, acceleration of gravity  $g = 0.80$  m/s<sup>2</sup>, and shear velocity  $v_s = 3.375 \cdot 10^{-2}$  m/s. The fluid has a viscosity  $\eta = 450$  mPa · s and density  $\rho_f = 1446 \frac{\text{kg}}{\text{m}^3}$ . This visualization is a typical example for a system that has reached a steady state: All particles have fallen to the ground due to the exerted gravitational force and most of the system has no particles [38]

$R = 1.125 \cdot 10^{-4}$  m. The system size is  $1.83 \cdot 10^{-3} \times 1.83 \cdot 10^{-3} \times 3.375 \cdot 10^{-3}$  m which corresponds to a lattice size of  $32 \times 32 \times 59$ . The density of the fluid is set to  $\rho_f = 1446 \frac{\text{kg}}{\text{m}^3}$ , and its viscosity is  $\eta = 450$  mPa · s. The walls at the top and the bottom are sheared with a relative velocity  $v_s = 3.375 \cdot 10^{-2}$  m/s. Figure 7 is a representative visualization of our simulation data and demonstrates that after the system has reached its steady state, all particles have fallen to the ground due to the influence of the gravitational force. Most of the simulation volume is free of particles.

In order to quantitatively characterize structuring effects, we calculate the particle density profile of the system by dividing the whole system into layers parallel to the walls and calculating a partial volume  $V_{ij}$  for each particle  $i$  crossing such a layer  $j$ . The scalar  $V_{ij}$  is given by the volume fraction of particle  $i$  that is part of layer  $j$ :

$$V_{ij} = \pi \left( R^2 (R_{ij}^{\max} - R_{ij}^{\min}) - \frac{1}{3} (R_{ij}^{\max} - R_{ij}^{\min}) \right) \quad (27)$$

If the component  $r_{i,z}$  perpendicular to the wall of the radius vector  $\mathbf{r}_i$  of the center of sphere  $i$  lies between  $r_j^{\min}$  and  $r_j^{\max}$ , we have

$$\begin{aligned} r_j^{\min} &= \left( j - \frac{1}{2} \right) \Delta L_z - R, \\ r_j^{\max} &= \left( j + \frac{1}{2} \right) \Delta L_z + R, \end{aligned}$$

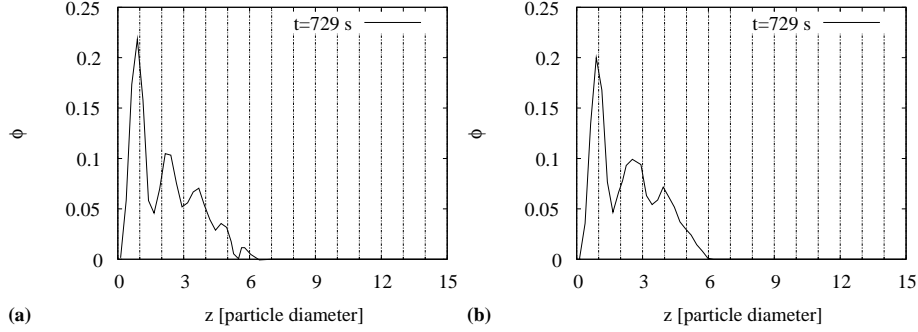


**Fig. 8.** Density profiles from simulations with two different shear rates  $\gamma = 10 \text{ s}^{-1}$  (a) and  $\gamma = 1 \text{ s}^{-1}$  (b). Other parameters are equal to those given in Fig. 7. (a) shows five peaks with separations about one particle diameter, which reveal the forming of particle layers. The number of particles per layer is decreasing with increasing distance to the wall, and the change in particle numbers is caused by gravity which is directed perpendicular to the wall at  $z = 0$ . Although we used the same gravity and particle numbers, there are only three peaks in (b) and their width is higher than in (a), demonstrating that the structuring effects strongly relate to the shear rate

and

$$R_{ij}^{\max} = \begin{cases} R & \text{if } r_{i,z} + R < r_j^{\max} \\ r_j^{\max} - r_{i,z} & \text{else} \end{cases},$$

$$R_{ij}^{\min} = \begin{cases} -R & \text{if } r_{i,z} - R > r_j^{\min} \\ r_j^{\min} - r_{i,z} & \text{else} \end{cases}.$$

Finally, the sum of all weights associated with a layer is divided by the volume of the layer

$$\phi_j = \frac{1}{L_x \cdot L_y \cdot \Delta L_z} \sum_{i=1}^N v_{ij}, \quad \Delta L_z = \frac{L_z}{M}, \quad (28)$$

with  $L_x, L_y$  being the system dimensions between periodic boundaries,  $L_z$  the distance between walls,  $M$  the number of layers, and  $\Delta L_z$  the width of a single layer.

Density profiles calculated by this means for systems with two different shear rates  $\gamma = 10 \text{ s}^{-1}$  and  $\gamma = 1 \text{ s}^{-1}$  are presented in Fig. 8. All other parameters are equal to the set given in the last paragraph. The peaks in Fig. 8 demonstrate that at certain distances from the wall the number of particles is substantially higher than at other positions. The first peak in both figures is slightly below one particle diameter, which can be explained by a lubricating fluid film between the first layer and the wall which is slightly thinner than one particle radius. Due to the small amount of particles, time dependent fluctuations of the width of the lubricating layer cannot be neglected and

a calculation of the exact value is not possible. The five peaks in Fig. 8a have similar distances which are equal to one particle diameter. These peaks can be explained by closely packed parallel layers of particles. Due to the linear velocity profile in  $z$ -direction of the fluid flow, every layer adopts the local velocity of the fluid resulting in a relative velocity difference between two layers of about  $2R\gamma$ . These layers stay stable in time with only a small number of particles being able to be exchanged between them.

Figure 8b only shows three peaks with larger distances than in Fig. 8a. However, the average slope of the profile is identical for both shear rates. For smaller shear rates, velocity differences between individual layers are smaller, too. As a result, particles feel less resistance while moving from one layer to another. Every inter-layer transition distorts the well defined peak structure of the density distribution resulting in only three clearly visible peaks in Fig. 8b.

With changing time, the first peak stays constant for both shear rates. The shape, number and position of all other peaks is slightly changing in time.

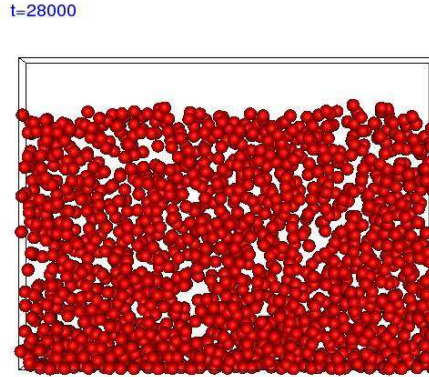


**Fig. 9.** A snapshot of a suspension with 1536 spheres after 28000 timesteps used to gain statistics of particle velocity distributions

We are currently investigating the occurrence of non-Gaussian velocity distributions of particles for higher particle densities and higher shear rates. For this, improvements of the method are mandatory in order to prevent instabilities of the simulation. By utilizing an implicit scheme for the update of the particle velocities [43, 54] we are able to overcome artefacts caused by numerical inaccuracies at high volume fractions or shear rates. Figure 9 shows a snapshot of a system containing 1536 particles after 28000 timesteps.

The lattice Boltzmann has been extended in order to include thermal fluctuations [43, 2]. With these modifications the method is another candidate to simulate suspensions where Brownian motion cannot be neglected.

## 4 Plug Conveying in Vertical or Horizontal Tubes: a Coarse Grained Model for the Fluid Flow

### 4.1 Model Description

Another approach to modeling two phase flow is to course-grain the fluid, so that it is resolved on a length scale larger than the grains. The advantage is that much larger systems can be treated, but the disadvantage is that this coarse-graining is justified only in certain situations. One of those situations is when the density of the fluid is small compared to that of the grains, and the Reynolds number of the grains is small. It is then possible to neglect the inertia of the fluid, which means that all momentum is contained in the grains. The fluid transfers momentum between grains, but stores no momentum itself. And when the Reynolds number of the grains is small, one can treat the granulate phase as a moving porous medium. In the following, we present the model in more detail.

#### Gas Model

The model for the gas simulation was first introduced by McNamara and Flekkøy [52] and has been implemented for the two-dimensional case to simulate the rising of bubbles within a fluidized bed. We developed a three-dimensional version of this algorithm.

The algorithm is based on the mass conservation of the gas and the granular medium. Conservation of grains implies that the density  $\varrho_p$  of the granular medium obeys

$$\frac{\partial \varrho_p}{\partial t} + \nabla \cdot (\mathbf{u} \varrho_p) = 0, \quad \varrho_p = \varrho_s(1 - \phi), \quad (29)$$

where  $\varrho_p$  is the mass density of the material making up the particles, the porosity of the medium is  $\phi$  (i.e. the fraction of the space available to the gas), and the velocity of the granulate is  $\mathbf{u}$ .

The mass conservation equation for the gas is

$$\frac{\partial \varrho_g}{\partial t} + \nabla \cdot (\mathbf{v}_g \varrho_g) = 0, \quad \varrho_g \propto \phi P, \quad (30)$$

where  $\varrho_g$  is the mass density of the gas averaged over the total volume of the granular medium and  $\mathbf{v}_g$  its velocity. This equation can be transformed into a differential equation for the gas pressure  $P$  using the ideal gas equation, together with the assumption of uniform temperature.

The velocity  $\mathbf{v}_g$  of the gas is related to the granulate velocity  $\mathbf{u}$  through the d'Arcy relation:

$$-\nabla P = \frac{\eta}{\kappa(\phi)}\phi(\mathbf{v}_g - \mathbf{u}), \quad (31)$$

where  $\eta$  is the dynamic viscosity of the air and  $\kappa$  is the permeability of the granular medium. This relation was first given by d'Arcy in 1856 [12]. The d'Arcy relation is preferred here over the Ergun equation, because it is linear in the velocity. This makes the simplification steps done later possible. For the permeability  $\kappa$  the Carman-Kozeny relation [8] was chosen, which provides a relation between the porosity  $\phi$ , the particle diameter  $d$  and the permeability of a granular medium of monodisperse spheres,

$$\kappa(\phi) = \frac{d^2\phi^3}{180(1-\phi)^2}. \quad (32)$$

Combining (29), (30) and (31) results in a nonlinear differential equation for the gas pressure:

$$\phi\left(\frac{\partial P}{\partial t} + \mathbf{u}\nabla P\right) = \nabla\left(P\frac{\kappa(\phi)}{\eta}\nabla P\right) - P\nabla\mathbf{u}. \quad (33)$$

After linearizing around the normal atmospheric pressure  $P_0$  the resulting differential equation only depends on the relative pressure  $P'$  ( $P = P_0 + P'$ ), the porosity  $\phi$  and the granular velocity  $\mathbf{u}$ , which can be derived from the particle simulation, and three constants: the viscosity  $\eta$ , the particle diameter  $d$  and the pressure  $P_0$ :

$$\frac{\partial P'}{\partial t} = \frac{P_0}{\eta\phi}\nabla(\kappa(\phi)\nabla P') - \frac{P_0}{\phi}\nabla\mathbf{u}. \quad (34)$$

This differential equation can be interpreted as a diffusion equation with a diffusion constant  $D = \phi\kappa(\phi)/\eta$ . The equation is solved numerically, using a Crank-Nickelson approach for the discretization. Each dimension is integrated separately.

### Granulate Algorithm

The model for the granular medium simulates each grain individually using a discrete element simulation (DES). For the implementation of the discrete element simulation we used a version of the molecular dynamics method described by Cundall [11]. The particles are approximated as monodisperse spheres, rotations in three dimensions are taken into account.

The equation of motion for an individual particle is

$$m\ddot{\mathbf{x}} = m\mathbf{g} + \mathbf{F}_c - \frac{m\nabla P}{\rho_s(1-\phi)}, \quad (35)$$

where  $m$  is the mass of a particle,  $\mathbf{g}$  the gravitation constant and  $\mathbf{F}_c$  the sum over all contact forces. The last term, the drag force, is assumed to be a

volume force given by the pressure drop  $\nabla P$  and the local mass density of the granular medium  $\varrho_s(1 - \phi)$ , which is valid for monodisperse granular media.

The interaction between two particles in contact is given by two force components: a normal and a tangential component with respect to the particle surface. The normal force is the sum of a repulsive elastic force (Hooke's law) and a viscous damping. The tangential force opposes the relative tangential motion and is proportional to the normal force (sliding Coulomb friction) or proportional to the relative tangential velocity (viscous damping). Viscous damping is used only for small relative tangential velocities.

### Gas-Grain Interaction

The simulation method uses both a continuum and a discrete element approach. While the gas algorithm uses fields, which are discretized on a cubic grid, the granulate algorithm describes particles in a continuum. A mapping is needed for the algorithms to interact. For the mapping a tent function  $F(\mathbf{r})$  is used:

$$F(\mathbf{r}) = f(x)f(y)f(z), \quad f(x) = \begin{cases} 1 - |x/l|, & |x/l| \leq 1, \\ 0, & 1 < |x/l|, \end{cases} \quad (36)$$

where  $l$  is the grid constant used for the discretization of the gas simulation.

For the gas algorithm the porosity  $\phi_j$  and the granular velocity  $\mathbf{u}_j$  must be derived from the particle positions  $\mathbf{r}_i$  and velocities  $\mathbf{v}_i$ , where  $i$  is the index of particle and  $j$  is the index for the grid node. The tent function distributes the particle properties around the particle position smoothly on the grid:

$$\phi_j = 1 - \sum_i F(\mathbf{r}_i - \mathbf{r}_j), \quad \mathbf{u}_j = \frac{1}{1 - \phi_j} \sum_i \mathbf{v}_i F(\mathbf{r}_i - \mathbf{r}_j), \quad (37)$$

where  $r_j$  is the position of the grid point and the sum is taken over all particles.

For the computation of the drag force on a particle the pressure drop  $\nabla P_i$  and the porosity  $\phi_i$  at the position of the particle are needed. These can be obtained by a linear interpolation of the fields  $\nabla P_j$  and  $\phi_j$  from the gas algorithm:

$$\phi_i = \sum_j \phi_j F(\mathbf{r}_j - \mathbf{r}_i), \quad \nabla P_i = \sum_j \nabla P_j F(\mathbf{r}_j - \mathbf{r}_i), \quad (38)$$

where the sum is taken over all grid points. Note that  $\nabla P_i$  is a continuous function of the particle position  $\mathbf{r}_i$ . There are no discontinuities at all boundaries.

## 4.2 Application to Plug Conveying

This method was applied to study plug conveying in both vertical [66] and horizontal [67] tubes. Plug conveying is a special case of pneumatic conveying,



where grains are driven through pipes by air flow. Plug conveying occurs when the flux of grains through the pipe is relatively high. Currently plug conveying is gaining importance in industry, because it causes a lower product degradation and pipeline erosion than dilute phase conveying.

Unfortunately, current models [39, 65] of plug conveying disagree even on the prediction of such basic quantities as the pressure drop and the total mass flow, and these quantities have a great impact in industrial applications. One of the reasons for the lack of valid models is that it is difficult to study plugs experimentally in a detailed way. Usually experimental setups are limited to the measurement of the local pressure drop, the total mass flux and the velocity of plugs. Simulational studies are handicapped by the high computational costs for solving the gas flow and the particle-particle interaction, and are therefore mostly limited to two dimensions.

Using the above-described method, we were able to provide a detailed view of plugs. This approach provides access to important parameters like the porosity and velocity of the granulate and the shear stress on the wall at relatively low computational costs. Contrary to the experiments, it is possible to access these parameters at high spatial resolution and without influencing the process of transportation at all. Additional to plug profiles, characteristic curves of the pressure drop and the influence of simulation parameters can be measured.

### 4.3 Results

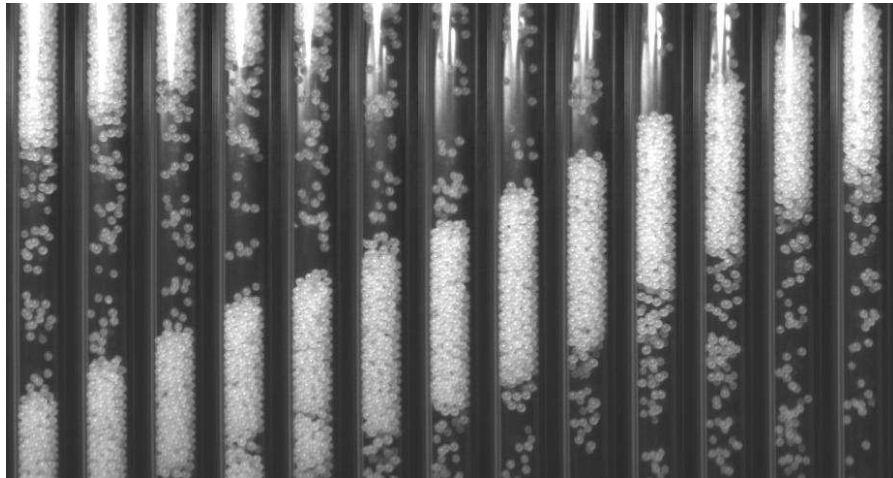


**Fig. 10.** A series of photos showing a plug moving upwards. The height of the shown tube is 9 cm, the frame rate is 30 Hz

In Fig. 10, we show a series of photos of plug conveying taken by Karl Sommer and Gerhard Niederreiter of TU München. The particles are wax beads of diameter  $d = 1.41$  mm, density  $\rho_s = 937$  kg/m<sup>3</sup> and a Coulomb coefficient of 0.21. The experimental transport channel is a vertical tube (PMMA) of length  $l = 1.01$  m and of internal diameter  $D_t = 7$  mm. The air is injected at a constant flow rate of  $2.2$  ℓ/min at the bottom of the tube. As one can easily see, grains travel in clusters up the tube.

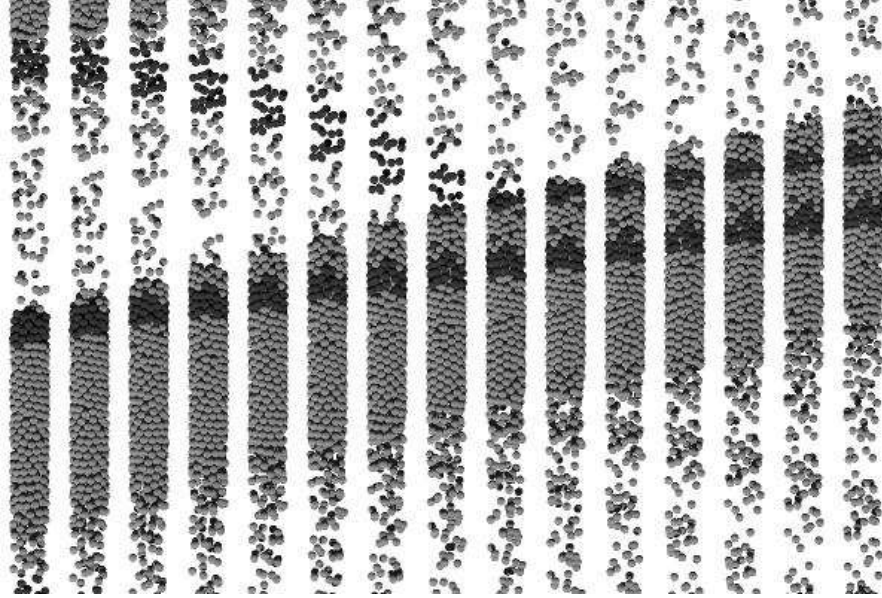


**Fig. 11.** A series of simulation snapshots showing a plug moving upwards. The height of the shown tube is 12 cm, the frame rate is 100 Hz

The simulations were carried out in a system that matched as closely as possible the experimental one. The same mode of transport was observed, as shown in Fig. 11. Not only is there a qualitative resemblance between Figs. 10 and 11, but the simulations give the same value for the pressure drop as the experiments. The success of the model permitted a thorough study of the plugs to be carried out. For example, so-called “characteristic curves”, where pressure drop is displayed as a function of gas velocity, could be calculated. The simulations also allow the study of the effects of parameters not easily controlled experimentally, such as the air viscosity and particle friction. The speed, density, size, and number of plugs were analyzed. In addition, the detailed structure of plugs could be studied. For example, the variation of density, velocity, and different components of the stress tensor were evaluated inside the plugs. All this information should help researchers to develop better models of plug conveying.

## 5 Conclusion

In this paper we have discussed the properties of various simulation techniques for particles in fluids and demonstrated that there is no perfect candidate that is able to simulate all systems of interest and to utilize the available resources as efficient as possible. For each individual problem, one has to choose the method of choice carefully: while stochastic rotation dynamics is well suited to simulate systems like clay-like colloids where Brownian motion is important, the lattice Boltzmann method is not able to resolve the stochastic motion of the particles without modifications of the method. However, in cases where thermodynamic fluctuations are neglectably small, this approach is much more efficient than stochastic rotation dynamics. Like conventional Navier-Stokes solvers, the fluid flow can be resolved in great detail, but the lattice Boltzmann method is much easier to implement and to parallelize. It is of particular advantage if complicated boundary conditions like non-spherical particles or complex channel geometries come into play. The implementation of Navier-Stokes solvers on the other hand can be based on a long-standing and widespread experience with these techniques allowing to create very efficient solvers. In macroscopic systems like the movement of granular particles in air, the exact properties of the flow field are not necessary to understand experimentally observable parameters. Therefore, computationally much less demanding techniques like a coarse-grained description of the fluid should be applied.

## Acknowledgements

We would like to thank all former members of the group who contributed to the projects related to the simulation of particles in fluids.

## References

1. A. Sierou and J.F. Brady. Accelerated stokesian dynamics simulations. *J. Fluid Mech.*, 448:115–146, 2001.
2. R. Adhikari, M. E. Cates, K. Stratford, and A. Wagner. Fluctuating lattice boltzmann. *condmat/0402598*, 2005.
3. P. Ahlrichs, R. Everaers, and B. Dünweg. Screening of hydrodynamic interactions in semidilute polymer solutions: A computer simulation study. *Phys. Rev. E*, 64(4):040501, 2001.
4. M. P. Allen and D. J. Tildesley. *Computer simulation of liquids*. Oxford Science Publications. Clarendon Press, 1987.
5. P. L. Bhatnagar, E. P. Gross, and M. Krook. Model for collision processes in gases. I. Small amplitude processes in charged and neutral one-component systems. *Phys. Rev.*, 94(3):511–525, 1954.

6. L. Bocquet, E. Trizac, and M. Aubouy. Effective charge saturation in colloidal suspensions. *J. Chem. Phys.*, 117:8138, 2002.
7. E. S. Boek, P. V. Coveney, H. N. W. Lekkerkerker, and P. van der Schoot. Simulating the rheology of dense colloidal suspensions using dissipative particle dynamics. *Phys. Rev. E*, 55(3):3124–3133, 1997.
8. P. Carman. Fluid flow through granular beds. *Trans. Inst. Chem. Engng.*, 26:150–166, 1937.
9. S. Chapman and T. G. Cowling. *The Mathematical Theory of Non-uniform Gases*. Cambridge University Press, second edition, 1952.
10. S. Chen and G. Doolen. Lattice-boltzmann method for fluid flows. *Ann. Rev. Fluid Mech.*, 30:329–364, 1998.
11. P. Cundall and D. Strack. Discrete numerical-model for granular assemblies. *Geotechnique*, 29:47–65, 1979.
12. H. d’Arcy. *Les fontaines publiques de la ville de Dijon*. Victor Dalmont, 1856.
13. P. Español. A fluid particle model. *Phys. Rev. E*, 57(3):2390–2948, 1998.
14. P. Español and P. Warren. Statistical mechanics of dissipative particle dynamics. *Europhys. Lett.*, 30(4):191–196, 1995.
15. E. Falck, J. M. Lahtinen, I. Vattulainen, and T. Ala-Nissila. Influence of hydrodynamics on many-particle diffusion in 2d colloidal suspensions. *Eur. Phys. J. E*, 13:267–275, 2004.
16. A. Fogelson and C. Peskin. A fast numerical method for solving the three-dimensional stokes equations in the presence of suspended particles. *J. Comput. Phys.*, 79:50, 1988.
17. F. Fonseca and H. J. Herrmann. Sedimentation of oblate ellipsoids at low and moderate reynolds numbers. *Physica A*, 342:447–461, 2004.
18. F. Fonseca and H. J. Herrmann. Simulation of the sedimentation of a falling oblate ellipsoid. *Physica A*, 345:341–355, 2005.
19. U. Frisch, D. d’Humières, B. Hasslacher, P. Lallemand, Y. Pomeau, and J.-P. Rivet. Lattice gas hydrodynamics in two and three dimensions. *Complex Systems*, 1:649–707, 1987.
20. U. Frisch, B. Hasslacher, and Y. Pomeau. Lattice-gas automata for the Navier-Stokes equation. *Phys. Rev. Lett.*, 56(14):1505–1508, 1986.
21. G. Bossis and J.F. Brady. Dynamic simulation of sheared suspensions. i. general method. *J. Chem. Phys.*, 80(10):5141–5154, 1984.
22. J. Harting, M. Harvey, J. Chin, M. Venturoli, and P. V. Coveney. Large-scale lattice boltzmann simulations of complex fluids: advances through the advent of computational grids. *Phil. Trans. R. Soc. A*, 363:1895–1915, 2005.
23. M. Hecht, J. Harting, M. Bier, J. Reinshagen, and H. J. Herrmann. Shear viscosity of clay-like colloids: Computer simulations and experimental verification. *submitted to Phys. Rev. E*, 2006. cond-mat/0601413.
24. M. Hecht, J. Harting, T. Ihle, and H. J. Herrmann. Simulation of claylike colloids. *Physical Review E*, 72:011408, 2005.
25. K. Höfler and S. Schwarzer. Navier-stokes simulation with constraint forces: Finite-difference method for particle-laden flows and complex geometries. *Phys. Rev. E*, 61:7146, 2000.
26. R. J. Hunter. *Foundations of colloid science*. Oxford University Press, 2001.
27. M. Hütter. *Brownian Dynamics Simulation of Stable and of Coagulating Colloids in Aqueous Suspension*. PhD thesis, Swiss Federal Institute of Technology Zurich, 1999.

28. M. Hütter. Local structure evolution in particle network formation studied by brownian dynamics simulation. *Journal of Colloid and Interface Science*, 231:337–350, 2000.
29. T. Ihle and D. M. Kroll. Stochastic rotation dynamics: A galilean-invariant mesoscopic model for fluid flow. *Phys. Rev. E*, 63:020201(R), 2001.
30. T. Ihle and D. M. Kroll. Stochastic rotation dynamics i: Formalism, galilean invariance, green-kubo relations. *Phys. Rev. E*, 67:066705, 2003.
31. T. Ihle and D. M. Kroll. Stochastic rotation dynamics ii: Transport coefficients, numerics, long time tails. *Phys. Rev. E*, 67:066706, 2003.
32. T. Ihle, E. Tuzel, and D. M. Kroll. Resummed green-kubo relations for a fluctuating fluid-particle model. *Phys. Rev. E*, 70:035701(R), 2004.
33. Y. Inoue, Y. Chen, and H. Ohashi. Development of a simulation model for solid objects suspended in a fluctuating fluid. *J. Stat. Phys.*, 107(1):85–100, 2002.
34. J.F. Brady and G. Bossis. Stokesian dynamics. *Ann. Rev. Fluid Mech.*, 20:111–157, 1988.
35. J.R. Melrose and R.C. Ball. “contact networks” in continuously shear thickening colloids. *J. Rheo.*, 48(5):961–978, 2004.
36. J.R. Melrose and R.C. Ball. Continuous shear thickening transitions in model concentrated colloids – the role of inter-particle forces. *Journal of Rheology*, 48(5):937–960, 2004.
37. N. Kikuchi, C. M. Pooley, J. F. Ryder, and J. M. Yeomans. Transport coefficients of a mesoscopic fluid dynamics model. *J. Chem. Phys.*, 119(12):6388–95, 2003.
38. A. Komnik, J. Harting, and H. J. Herrmann. Transport phenomena and structuring in shear flow of suspensions near solid walls. *J. Stat. Mech: Theor. Exp.*, P12003, 2004.
39. K. Konrad and T. Totah. Vertical pneumatic conveying or particle plug. *Canadian Journal of Chemical Engineering*, 67:245–252, 1989.
40. E. Kuusela, K. Höfler, and S. Schwarzer. Computation of settling speed and orientation distribution in suspensions of prolate spheroids. *J. Eng. Math.*, 41:221, 2001.
41. A. J. C. Ladd. Numerical simulations of particulate suspensions via a discretized boltzmann equation. part 1. theoretical foundation. *J. Fluid Mech.*, 271:285–309, 1994.
42. A. J. C. Ladd. Numerical simulations of particulate suspensions via a discretized boltzmann equation. part 2. numerical results. *J. Fluid Mech.*, 271:311–339, 1994.
43. A. J. C. Ladd and R. Verberg. Lattice-boltzmann simulations of particle-fluid suspensions. *J. Stat. Phys.*, 104(5):1191, 2001.
44. G. Lagaly, O. Schulz, and R. Zimehl. *Dispersionen und Emulsionen*. Dr. Dietrich Steinkopff Verlag, Darmstadt, Germany, 1997.
45. A. Lamura, G. Gompper, T. Ihle, and D. M. Kroll. Multi-particle-collision dynamics: Flow around a circular and a square cylinder. *Eur. Phys. Lett*, 56:319, 2001.
46. L.E. Silbert, J.R. Melrose, and R.C. Ball. Colloidal microdynamics: Pair-drag simulations of model-concentrated aggregated systems. *Phys. Rev. E*, 56(6):7067–7077, 1997.
47. J. A. Lewis. Colloidal processing of ceramics. *J. Am. Ceram. Soc.*, 83:2341–59, 2000.
48. M. Loewenberg and E. Hinch. Numerical simulation of a concentrated emulsion in shear flow. *J. Fluid. Mech.*, 321:395–419, 1996.

49. J. Mahanty and B. W. Ninham. *Dispersion Forces*. Academic Press, London, 1996.
50. A. Malevanets and R. Kapral. Mesoscopic model for solvent dynamics. *J. Chem. Phys.*, 110:8605, 1999.
51. A. Malevanets and R. Kapral. Solute dynamics in mesoscale solvent. *J. Chem. Phys.*, 112:7260, 2000.
52. S. McNamara, E. Flekkøy, and K. Måløy. Grains and gas flow: Molecular dynamics with hydrodynamic interaction. *Phys. Rev. E*, 61:658–670, 2000.
53. I. D. Morrison and S. Ross. *Colloidal Dispersions: Suspensions, Emulsions and Foams*. John Wiley and Sons, New York, 2002.
54. N. Q. Nguyen and A. J. C. Ladd. Lubrication corrections for lattice-boltzmann simulations of particle suspensions. *Phys. Rev. E*, 66(4):046708, 2002.
55. R. Oberacker, J. Reinshagen, H. von Both, and M. J. Hoffmann. Ceramic slurries with bimodal particle size distributions: Rheology, suspension structure and behaviour during pressure filtration. *Ceramic Transactions*, 112:179–184, 2001.
56. P. Mijatović. Bewegung asymmetrischer Teilchen unter stochastischen Kräften. Master-thesis, Universität Stuttgart, 2002.
57. D. Petera and M. Muthukumar. Brownian dynamics simulation of bead-rod chains under shear with hydrodynamic interaction. *J. Chem. Phys.*, 111(16):7614–7623, 1999.
58. J. Reinshagen, R. C. D. Cruz, R. Oberacker, and J. Hoffmann. Electrostatically stabilized alumina suspensions with defined interparticle potentials: I. influence of salt concentration on suspension conductivity and rheology. *submitted*, 2005.
59. S. Richter and G. Huber. Resonant column experiments with fine-grained model material - evidence of particle surface forces. *Granular Matter*, 5:121–128, 2003.
60. M. Ripoll, K. Mussawisade, R. G. Winkler, and G. Gompper. Low-reynolds-number hydrodynamics of complex fluids by multi-particle-collision dynamics. *Europhys. Lett.*, 68:106–112, 2004.
61. W. B. Russel, D. A. Saville, and W. Schowalter. *Colloidal Dispersions*. Cambridge Univ. Press., Cambridge, 1995.
62. K. S. Schmitz. *Macroions in Solution and Colloidal Suspension*. John Wiley and Sons, New York, 1993.
63. S. Schwarzer, K. Höfler, and B. Wachmann. Simulation of hindered settling in bidisperse suspensions of rigid spheres. *Comp. Phys. Comm.*, 268:121–122, 1999.
64. D. J. Shaw. *Introduction to Colloid and Surface Chemistry*. Butterworth-Heinemann Ltd, Oxford, 1992.
65. W. Siegel. *Pneumatische Förderung*. Vogel, 1991.
66. M. Strauß, H. Herrmann, S. McNamara, G. Niederreiter, and K. Sommer. Plug conveying in a vertical tube. *Particle Technology*, submitted, 2005.
67. M. Strauß, S. McNamara, and H. Herrmann. Plug conveying in a horizontal tube. *Granular Matter*, accepted, 2006.
68. T. Pöschel. Granular material flowing down an inclined chute: a molecular dynamics simulation. *J. Phys. II*, 3(1):27–40, 1993.
69. T.N. Phung, J.F. Brady, and G. Bossis. Stokesian dynamics simulation of brownian suspensions. *J. Fluid Mech.*, 313:181–207, 1996.
70. E. Tuzel, M. Strauss, T. Ihle, and D. M. Kroll. Transport coefficients in three dimensional stochastic rotation dynamics. *Phys. Rev. E*, 68:036701, 2003.
71. J. Vermant and M. J. Solomon. Flow-induced structure in colloidal suspensions. *J.Phys.: Condens. Matter*, 17:R187–R216, 2005.

72. B. Wachmann and S. Schwarzer. Three dimensional massively parallel computing of suspensions. *Int. J. of Modern Physics C*, 9:759–776, 1998.
73. G. Wang, P. Sarkar, and P. S. Nicholson. Surface chemistry and rheology of electrostatically (ionically) stabilized alumina suspensions in polar media. *J. Am. Ceram. Soc.*, 82(4):849–56, 1999.
74. R. G. Winkler, K. Mussawisade, M. Ripoll, and G. Gompper. Rod-like colloids and polymers in shear flow: a multi-particle-collision dynamics study. *J. of Physics-Condensed Matter*, 16(38):S3941–54, 2004.





